

Arrayed waveguide gratings in lithium tantalate integrated photonics

Shivaprasad U. Hulyal, Jianqi Hu, Chengli Wang, Jiachen Cai, Grigory Lihachev, and Tobias J. Kippenberg*
*Institute of Physics, Swiss Federal Institute of Technology Lausanne (EPFL), CH-1015 Lausanne, Switzerland and
 Institute of Electrical and Micro engineering, Swiss Federal Institute of Technology,
 Lausanne (EPFL), CH-1015 Lausanne, Switzerland*

Arrayed Waveguide Gratings (AWGs) are widely used photonic components for splitting and combining different wavelengths of light. They play a key role in wavelength division multiplexing (WDM) systems by enabling efficient routing of multiple data channels over a single optical fiber [1] and as a building block for various optical signal processing, computing, imaging, and spectroscopic applications [2–5]. Recently, there has been growing interest in integrating AWGs in ferroelectric material platforms, as the platform simultaneously provide efficient electro-optic modulation capability and thus hold the promise for fully integrated WDM transmitters. To date, several demonstrations have been made in the X-cut thin-film lithium niobate (LiNbO_3) platform [6–11], yet, the large anisotropy of LiNbO_3 complicates the design and degrades the performance of the AWGs. To address this limitation, we use the recently developed photonic integrated circuits (PICs) based on thin-film lithium tantalate (LiTaO_3) [12], a material with a similar Pockels coefficient as LiNbO_3 but significantly reduced optical anisotropy, as an alternative viable platform. In this work, we manufacture LiTaO_3 AWGs using deep ultraviolet lithography on a wafer-scale. The fabricated AWGs feature a channel spacing of 100 GHz, an insertion loss of < 4 dB and crosstalk of < -14 dB. In addition, we demonstrate a cyclic AWG, as well as a multiplexing and demultiplexing AWG pair for the first time on LiTaO_3 platform. The wafer-scale fabrication of these AWGs not only ensures uniformity and reproducibility, but also paves the way for realizing volume-manufactured integrated WDM transmitters in ferroelectric photonic integrated platforms.

I. INTRODUCTION

Integrated photonics leverages the broad bandwidth of optics, spanning from the visible to the mid-infrared, to enable advanced technologies such as optical telecommunications [13], precision metrology [14], and photonic computing [15]. Central to these applications are integrated components like wavelength division multiplexers (WDMs), which efficiently separate, route, and combine multiple optical signals [16]. For instance, WDMs can be used as both multiplexers and demultiplexers for data transmission of densely parallel channels over op-

tical fibers, thereby significantly enhancing bandwidth utilization and network capacity. Among others, arrayed waveguide gratings (AWGs), have become a building block due to their versatility and efficiency in wavelength routing and spectral analysis [17, 18]. They have been used for various photonics-based applications, ranging from communications [1], imaging [4], spectroscopy [5], sensing [19], to microwave photonics [2] and photonic computing [3].

Over the past decades, AWGs have been demonstrated on various photonic integrated platforms, including silica [20], silicon [21], silicon nitride [22], polymer [23], and indium phosphide [24]. More recently, significant efforts have been made to integrate AWGs in the lithium niobate on insulator (LNOI) platform [6–11], leveraging its exceptional electro-optic modulation capability [25, 26]. X-cut lithium niobate (LiNbO_3) is of particular interest, due to its ability to support low driving voltage, high-bandwidth electro-optic modulators [27, 28]. However, in the X-cut LiNbO_3 , the optical waveguides experience large orientation-dependent refractive indices. Such anisotropy poses challenges in realizing high-performance AWGs in the X-cut. To this end, aligning the symmetry axis of the AWGs along the 45° crystal axis has been shown to alleviate the issue by canceling the anisotropy [10]. Yet, this approach may complicate the overall layout and routing of photonic circuits, potentially increasing the device footprint. Any deviation from the optimal alignment may also reintroduce the anisotropic behavior, requiring tighter fabrication tolerances.

Recently, tightly confined photonic integrated circuits with low loss have been demonstrated in lithium tantalate on insulator (LTOI), using a diamond like carbon hardmask (DLC) [12]. Compared to LiNbO_3 , the integrated lithium tantalate (LiTaO_3) platform offers similar Pockels coefficient, while benefiting from lower wafer per cost due to its large-scale production in consumer electronics [29]. High speed optical modulators for communications have been demonstrated in this platform [30], with reduced bias drift [30, 31], higher damage threshold and wider bandgap. Most importantly, LiTaO_3 features more than ten-fold reduction in optical anisotropy relative to LiNbO_3 ($\Delta n_{\text{LT}} = 0.004$ versus $\Delta n_{\text{LN}} = -0.07$). This property of LiTaO_3 has facilitated the generation of ultra-broadband electro-optic frequency combs beyond the birefringence limit [32], and enables design of compact photonic integrated circuits with tight bend radii.

Here, by leveraging the reduced anisotropy of LiTaO_3 , we demonstrate AWGs on X-cut LiTaO_3 without having

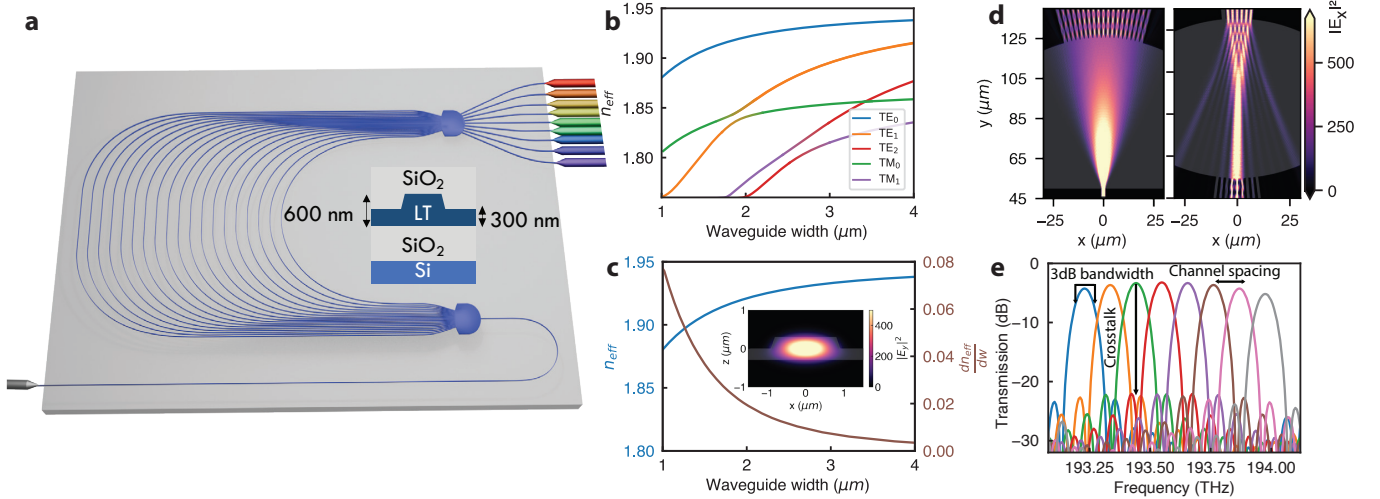


Figure 1. **Design and simulation of arrayed waveguide gratings based on LiTaO₃ photonic integrated circuits.** (a) Schematic diagram of the AWG. The inset shows the material stack. (b) Refractive index of various modes supported by partially etched LiTaO₃ waveguide. (c) Effective indices and the change in refractive indices at different waveguide widths of the TE₀ mode on LiTaO₃ waveguide. (d) (left panel) Simulation of light diffraction from the input waveguide into the star coupler, followed by coupling into arrayed waveguides, (right panel) Simulation of the light entering the output star coupler, after accumulating phase delays in the arrayed waveguides and constructively interfering at one of the output waveguides (the central waveguide is coupled for in-phase illumination). (e) Simulated transmission spectrum of the AWG.

to rely on rotational schemes or other intricate methods to counterbalance anisotropy. We fabricate AWGs for the first time at wafer scale on a ferroelectric material platform, achieving dense channel spacing, competitive insertion loss, and acceptable crosstalk and uniformity across different regions of the wafer. We use both Confocal and Rowland types of star couplers [33, 34], which render comparable AWG performance. In addition, we demonstrate a cyclic AWG, as well as a matched multiplexing and demultiplexing AWG pair for the first time to our knowledge. The wafer-scale fabrication of AWGs in a ferroelectric platform provides a scalable and cost-effective solution for on-chip optical communication and spectroscopic systems.

II. DESIGN AND SIMULATION

Figure 1a illustrates the schematic architecture of an AWG. At its core, an AWG comprises of an input star coupler, an array of waveguides with uniformly incremental path-length differences, and an output star coupler. Initially, the optical signal is injected into the input star coupler, where it undergoes in-plane diffraction, resulting in a fan-out of the light coupling into a number of radial paths. Each path then propagates through an individual waveguide in the array, where a constant length increment is meticulously maintained. This accumulated path-length difference imparts a progressive delay to the different copies of propagating light. Upon emerging from the waveguide array, the light enters the output star coupler, where the varying phases accumulated along dif-

ferent waveguides interact to produce constructive and destructive interference patterns. The resulting interference is such that light at specific wavelengths constructively interferes at designated output waveguides, effectively demultiplexing the spectral components of the input signal. Based on the arrangement of the waveguide apertures at the focal plane, the output star coupler can be classified into two primary configurations: Confocal and Rowland-type geometries. In the Confocal geometry, both the input and output waveguides are positioned along a circle with the same radius. While the Rowland geometry places the output waveguides on a circle with half that radius. In this work, both geometries are designed and fabricated in the thin-film LiTaO₃ platform.

The design parameters of an AWG—including focal length, delay length, free spectral range, dispersion, and diffraction order—are inherently interdependent (cf. Supplementary note 1). These parameters are intricately linked through the effective and group indices of the waveguides, rendering the AWG design process complex. The design of AWG starts by choosing an appropriate waveguide width. A waveguide width whose refractive index is not sensitive to fabrication imperfections nor mode mixing is used. From Figure 1b we choose a waveguide width in the multimode regime to minimize phase errors caused by sidewall roughness [35]. Figure 1c shows that the TE₀ is tolerant to the waveguide width variations for larger waveguide widths and hence we chose widths of 1.6 μm and 1.8 μm for the Confocal and Rowland AWGs, respectively. Additionally, we designed parabolic taper connecting the waveguides to the star coupler aperture (cf. Supplementary note 3), so as to achieve low-

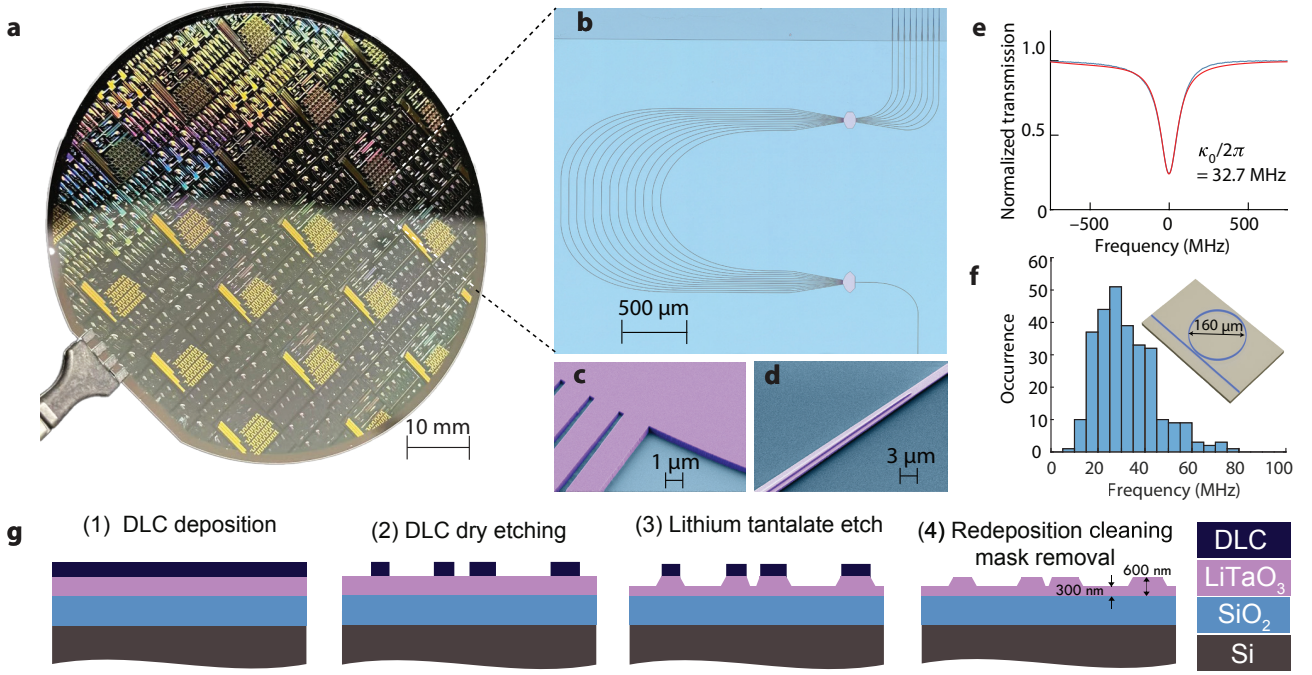


Figure 2. **Wafer-scale manufacturing of LTOI arrayed waveguide gratings.** (a) Optical image of a 4-inch wafer of LiTaO₃ integrated AWG following the fabrication processes. (b) Photo of the photonic chip comprising of the fabricated Confocal type configuration AWG. False-colored Scanning Electron Microscope (SEM) images of the arrayed aperture spacing, (c) arrayed waveguide aperture, (d) Double layered tapers. (e) Normalized resonance transmission spectrum of an optical microring resonator at 204.149 THz (blue curve: measured data; red curve: fitted response). (f) Statistical distribution of intrinsic loss, $\kappa_0/2\pi$. Mean $(\overline{\kappa_0}/2\pi) = 32.7 \text{ MHz}$, of the optical microring resonator. (g) Wafer-scale fabrication process flow.

loss mode transition [36]. These tapers play an essential role in efficiently coupling light between waveguides with different cross-sectional dimensions. The arrayed waveguides are uniformly bent with identical radii to ensure they remain parallel, and straight sections are subsequently added so that the outermost waveguides extend further than the inner ones. In our design, Euler bends [37] are incorporated into the arrayed waveguides to optimize the optical routing while mitigating propagation losses. Specifically, these bends are engineered with curvature radii of more than 300 μm , ensuring a smooth transition that maintains mode integrity and minimizes scattering effects. After that, there are again straight sections to make the appropriate incremental length offset. These waveguides are repeated to reach the output array aperture. In the output star coupler, interference between the optical fields determines the distribution of light into the output waveguides. For a given frequency, the superposition of phase-shifted waves results in constructive interference at specific locations, corresponding to the output channel positions.

The simulation of AWG (cf. Supplementary note 2) involves both analytical approaches and numerical modeling based on the finite-difference time-domain (FDTD) method [17, 34]. First, the light diffraction from the input star coupler and its coupling into arrayed waveguides are simulated using FDTD in Figure 1d (left). Next, the light

in each arrayed waveguide experiences a precise group delay determined by the calculated length difference between the waveguides. Finally, FDTD is used again to simulate the light propagation in the output star coupler. As shown in Figure 1d (right), at the center frequency where the light in the arrayed waveguides is in-phase, the light is mainly focused into the central output waveguide with slight leakage into adjacent waveguides leading to crosstalk. Depending on the input light frequency, the light is directed into different waveguides at the output aperture to form the transmission spectrum as shown in Figure 1e. This figure also illustrates the definitions of 3 dB bandwidth, channel spacing, and crosstalk for the AWG used in this work.

III. FABRICATION

A 4-inch (102 mm) LiTaO₃ wafer (Figure 2a) with a surface roughness of 0.25 nm and a non-uniformity of less than 30 nm is used to fabricate the AWGs (Figure 2b) [12]. The LTOI wafer stack comprises a 600 nm single-crystal LiTaO₃ layer, a 4.7 μm thermal SiO₂ buried oxide, and a 625 μm high-resistivity (10 $k\Omega \cdot \text{cm}$) silicon handle substrate. The LiTaO₃ photonic chips are fabricated based on 248 nm DUV stepper lithography (ASML PAS5500/350C) using a highly selective hard-

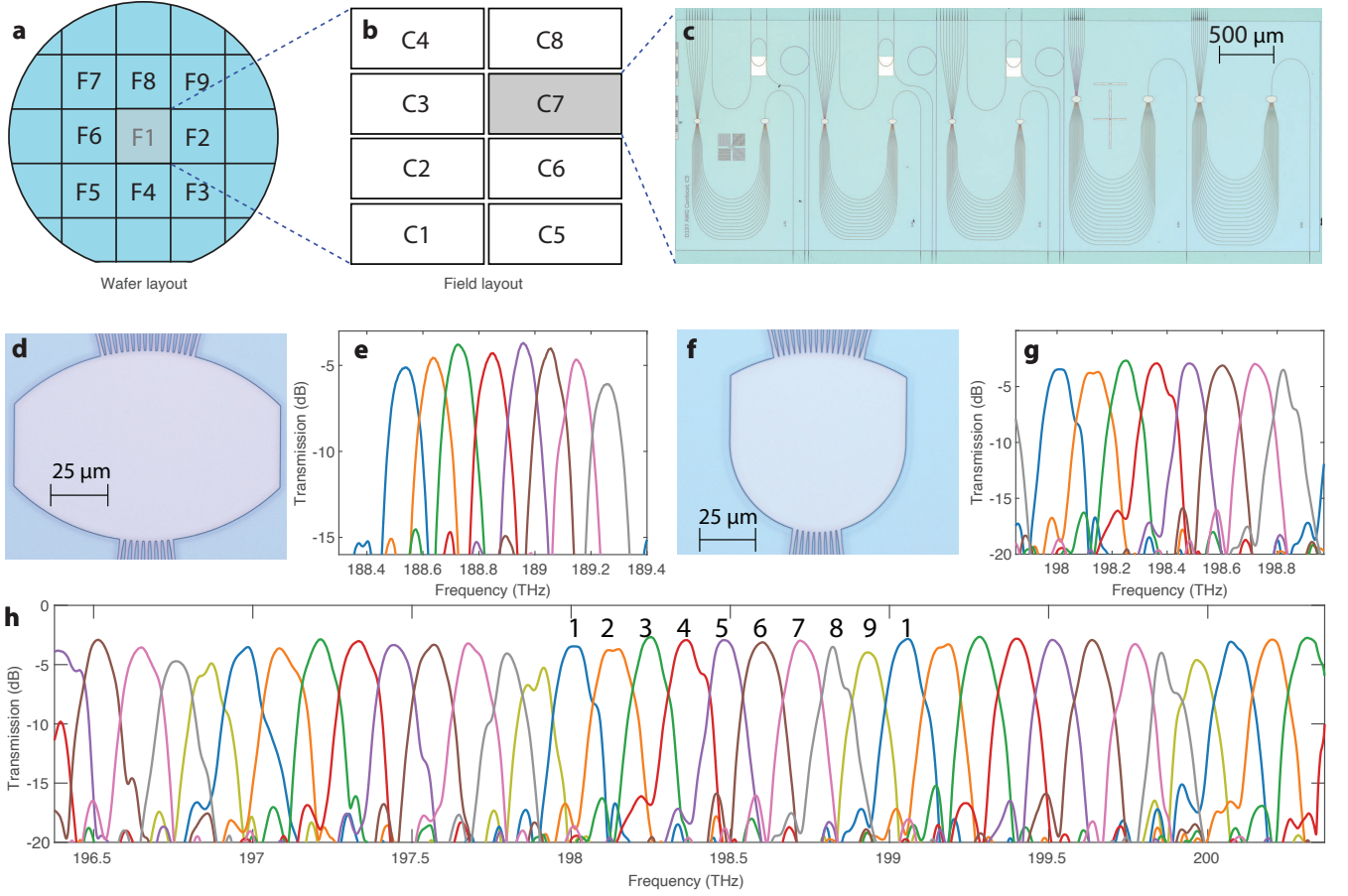


Figure 3. **Characterization of fabricated LiTaO₃ arrayed waveguide gratings.** (a) DUV stepper exposure layout. (b) The reticle design containing eight chips is uniformly exposed in discrete fields over a 4-inch wafer. (c) Photonic image of the fabricated chip containing five confocal 8-channel 100 GHz AWGs in a single chip. (d) Microscopic image of fabricated Confocal output star coupler. (e) Transmission spectrum of the 8-channel 100 GHz AWG (Device ID: D197_F5_C1_WG_203) with Confocal star couplers. (f) Microscopic image of fabricated Rowland output star coupler. (g) Transmission spectrum of the 8-channel 100 GHz AWG with Rowland star couplers (Device ID: D197_F1_C6_WG_301). (h) Cyclic AWG design with $1 \times 9 \times 100$ GHz (Device ID: D197_F1_C6_WG_301).

mask subtractive waveguide manufacturing process, with the DLC as the hardmask [12] (Figure 2g). The process begins with the DLC hard mask deposition. A multi-layer hard mask stack is deposited via plasma-enhanced chemical vapor deposition (PECVD), consisting of a 30 nm Si₃N₄ layer, a 480 nm DLC layer, and a top 60 nm Si₃N₄ layer. Waveguide patterns are initially transferred onto the DLC hard mask using an oxygen plasma etch in a reactive ion etching (RIE) system, taking advantage of the DLC's superior etch selectivity and robustness. Subsequently, the waveguide cores are etched into the LiTaO₃ layer using ion beam etching (IBE) in a Veeco Nexus IBE350 system. This step achieved an etch depth of approximately 300 nm, retaining a 300 nm-thick slab that is readily compatible with high-speed electro-optic modulation [38]. During IBE, amorphous re-deposited material may form on the sidewalls, and this residue is removed by a post-etch chemical cleaning step to ensure smooth and low-loss waveguide profiles as shown Fig-

ure 2c. An 800 nm SiO₂ cladding layer is deposited on the optical layer via a ICP-CVD system (PlasmaPro 100 ICP-CVD). Device separation is carried out through a multi-step release process: dry etching of the LiTaO₃ and SiO₂ layers using fluorine-based chemistry, followed by deep reactive-ion etching of the silicon carrier. This sequence yields smooth end facets suitable for efficient edge coupling via the double layer tapers to external light sources as depicted in Figure 2d. The double layer tapers are designed to enhance the transmission efficiency (3.7 dB fiber-to-fiber) by matching the mode fields of the lensed fiber and the taper (cf. Supplementary note 5).

IV. CHARACTERIZATION

After fabrication, we characterized the LiTaO₃ AWGs using tunable diode lasers calibrated with a self-referenced frequency comb (Menlo OFC-1500). To ensure

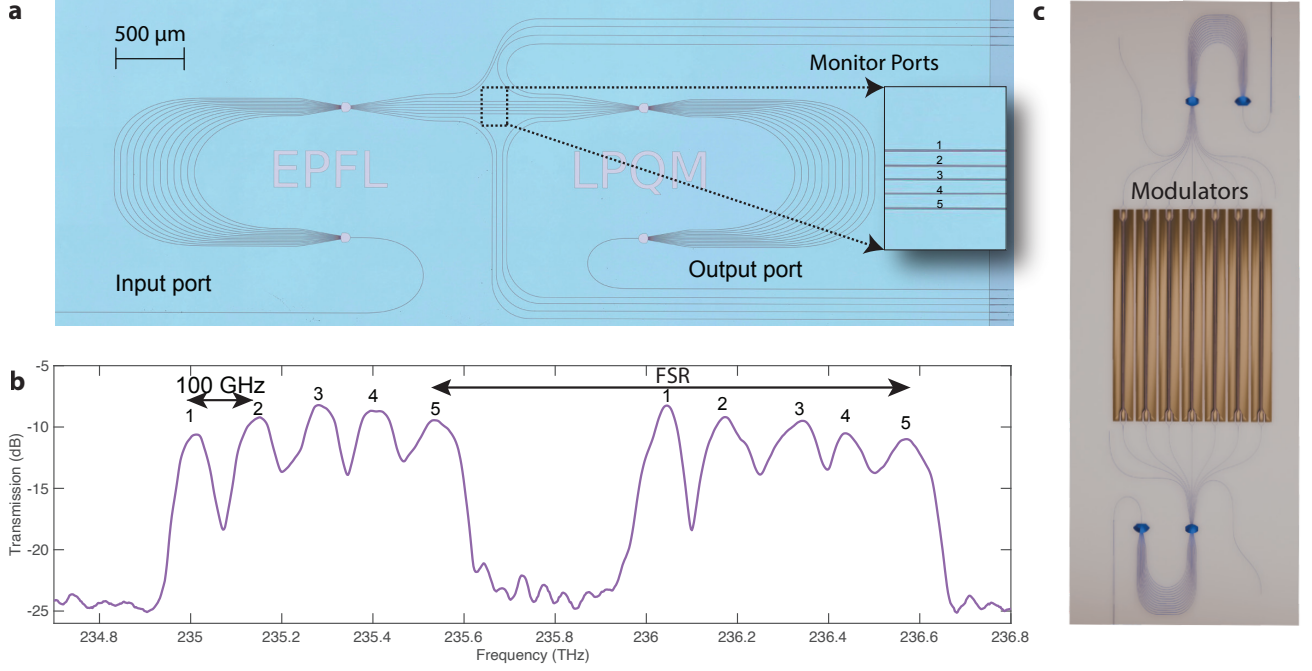


Figure 4. **Demonstration of multiplexing demultiplexing using arrayed waveguide grating pair.** (a) Microscope image of the fabricated (Device ID: D197_F6_C7_WG_305) passive cascaded configuration of two AWGs demonstrating spectral routing. The five outputs of the left AWG are directly connected to the five inputs of AWG on the right, creating a testbed for evaluating passive device characteristics. The inset shows the five ports. (b) Comb-calibrated characterized response showing the clear peaks corresponding to the five channels. (c) Concept of a fully integrated transmitter with modulators between two AWG to encode the data on LiTaO₃ platform.

a linear frequency scanning, we use the beating between the laser and the comb as a reference to calibrate the laser scan [39]. The propagation loss of LiTaO₃ waveguides are obtained by measuring the intrinsic loss rate $\kappa_0/2\pi$ of a LiTaO₃ microresonator in the same wafer, which gives $\kappa_0/2\pi = 32.7$ MHz corresponding to a propagation loss of 5.95 dB/m (Figure 2e and f). Figure 3a-c show the wafer and chip layout as well as an optical microscope image of the fabricated 8-channel AWGs with Confocal (Figure 3d) and Rowland (Figure 3f) configurations, both designed for a nominal 100 GHz channel spacing. The corresponding measured output spectra for the Confocal AWG are presented in Figure 3e, exhibiting an insertion loss of 6.14 ± 0.72 dB, 3-dB bandwidth of 101.92 ± 7.54 GHz, adjacent channel crosstalk of -13.38 ± 1.64 dB, and a measured channel spacing of 106.73 ± 8.38 GHz, where all uncertainties represent one standard deviation. In comparison, the spectra of the Rowland-type AWG, shown in Figure 3g, demonstrate an insertion loss of $3.16 \text{ dB} \pm 0.35$, 3-dB bandwidth of 92.14 ± 16.86 GHz, adjacent channel crosstalk of -14.67 ± 1.25 dB, and a channel spacing of 116.46 ± 13.58 GHz, also reported with one standard deviation uncertainty. These spectral responses are consistently observed across multiple fields of the wafer (cf. Supplementary note 4), underscoring the excellent reproducibility of AWG performance at the wafer-scale. Furthermore, the measured

results are in good agreement with the simulated spectra (Figure 1e), validating the effectiveness of the design and fabrication methodologies for both configurations. The AWG with the Rowland star coupler (Figure 3g) also exhibits the characteristics of a so-called "cyclic" or "colourless" AWG (Figure 3h) [40, 41]. That is, a signal that initially exits through the end output channel will reappear at the first output channel when its frequency is increased by an amount equal to the channel spacing of the AWG. Such a cyclic behaviour can be leveraged for a range of applications, particularly for 1×9 wavelength routing and optical add-drop multiplexers.

Next, we implement a pair of identical AWGs interconnected as shown in Fig. 4a. Specifically, five channels from the first AWG are routed to the second AWG, while remaining channels serve as monitoring ports. Figure 4b shows the characterization results of the device, clearly showing the spectral response of the five channels. Precise fabrication is crucial for this configuration to function properly; any deviations can lead to misalignment in the AWG transmission response, resulting in no detectable output. This multiplexing-demultiplexing configuration is a key step towards realizing a fully integrated LiTaO₃ WDM transmitter, as illustrated in Figure 4c, providing a path for future Tb/s-scale optical communication system.

CONCLUSION

In this work, we report the first demonstration of AWGs on thin-film LiTaO₃ based photonic integrated circuit platform. Notably, these AWGs operate passively, requiring neither active control nor complex design, but solely relying on the inherently low anisotropy of the material. Fabricated on X-cut LiTaO₃ that supports high-speed modulators, the AWGs achieve a channel spacing around 100 GHz, which aligns with the ITU grid standard and thereby paves the way for highly dense WDM transmitters on chip. Toward this goal, wafer-scale fabrication of AWGs is desired, offering a scalable, reproducible and cost-effective solution for volume manufacturing.

Besides its use in optical communications, the AWGs in X-cut LTOI platform also hold potential for many other photonic-based applications. Since superior electro-optic frequency combs have been developed in the ferroelectric platform [32, 42, 43], AWGs can combine monolithically with the comb, empowering on-chip comb-based microwave and optical signal processing [2], light ranging and detection [44], photonic computing [15], and quantum information processing [45]. In addition to the resonant electro-optic combs [32] and AWGs demonstrated in this work, the reduced anisotropy of LiTaO₃ may also

facilitate the development of other linear and nonlinear functionalities in this platform, e.g., the dispersion management module [46] and stimulated Brillouin scattering [47]. These building blocks would propel photonic systems in LTOI to new heights for next-generation communication and computing technologies.

Note: During the preparation of this manuscript another competing paper [48] was published.

Author Contributions: S.U.H. simulated and designed the devices. C.W., J.C. fabricated the device. S.U.H. carried out the measurements and analyzed the data with the help of J.H. T.J.K., J.H. supervised the project.

Funding Information and Disclaimer: This work was supported by Contract N660012424006 (NaPSAC) from the Defense Advanced Research Projects Agency (DARPA), Defense Sciences Office (DSO). It was further supported by the Swiss National Science Foundation under grant agreement No. 21649 (HEROIC). S.U.H. acknowledges support from Horizon Europe research and innovation programme under the Marie Skłodowska-Curie grant agreement No 101119968 (MicrocombSys) and from the Swiss State Secretariat for Education, Research and Innovation (SERI).

Acknowledgments: The samples were fabricated in the EPFL Center of MicroNanoTechnology (CMi).

Data Availability Statement: The code and data used to produce the plots within this work will be released on the repository Zenodo upon publication of this preprint.

Correspondence and requests for materials should be addressed to T.J.K.

* tobias.kippenberg@epfl.ch

- [1] S. Chandrasekhar, M. Zirngibl, A. Dentai, C. Joyner, F. Storz, C. Burrus, and L. Lunardi, Monolithic eight-wavelength demultiplexed receiver for dense wdm applications, *IEEE Photonics Technology Letters* **7**, 1342 (1995).
- [2] A. J. Metcalf, H.-J. Kim, D. E. Leaird, J. A. Jaramillo-Villegas, K. A. McKinzie, V. Lal, A. Hosseini, G. E. Hoefler, F. Kish, and A. M. Weiner, Integrated line-by-line optical pulse shaper for high-fidelity and rapidly reconfigurable rf-filtering, *Optics Express* **24**, 23925 (2016).
- [3] J. Cheng, C. Li, J. Dai, Y. Chu, X. Niu, X. Dong, and J.-J. He, Direct optical convolution computing based on arrayed waveguide grating router, *Laser & Photonics Reviews* **18**, 2301221 (2024).
- [4] E. A. Rank, R. Sentosa, D. J. Harper, M. Salas, A. Gaugutz, D. Seyringer, S. Nevlacsil, A. Maese-Novo, M. Eggeling, P. Muellner, *et al.*, Toward optical coherence tomography on a chip: in vivo three-dimensional human retinal imaging using photonic integrated circuit-based arrayed waveguide gratings, *Light: Science & Applications* **10**, 6 (2021).
- [5] P. Gatkine, S. Veilleux, Y. Hu, J. Bland-Hawthorn, and M. Dagenais, Arrayed waveguide grating spectrometers for astronomical applications: new results, *Optics express* **25**, 17918 (2017).
- [6] M. Prost, G. Liu, and S. B. Yoo, A compact thin-film lithium niobate platform with arrayed waveguide gratings and MMIs, in *2018 Optical Fiber Communications Conference and Exposition (OFC)* (IEEE, 2018) pp. 1–3.
- [7] Y. Yu, Z. Yu, Z. Zhang, H. K. Tsang, and X. Sun, Wavelength-division multiplexing on an etchless lithium niobate integrated platform, *ACS Photonics* **9**, 3253 (2022).
- [8] Z. Wang, Z. Fang, Z. Liu, Y. Liang, J. Liu, J. Yu, T. Huang, Y. Zhou, H. Zhang, M. Wang, and Y. Cheng, On-Chip Arrayed Waveguide Grating Fabricated on Thin-Film Lithium Niobate, *Advanced Photonics Research* **5**, 2300228 (2024).
- [9] H. Tu, Y. Zhang, G. Li, X. Dai, Y. Wu, Y. Zhang, H. Li, Q. Lu, M. Lu, and W. Guo, 100-Channel Arrayed Waveguide Grating Based on Thin Film Lithium Niobate on Insulator (LNOI), *Journal of Lightwave Technology* **42**, 4519 (2024).
- [10] J. Yi *et al.*, Anisotropy-free arrayed waveguide gratings on X-cut thin film lithium niobate platform of in-plane anisotropy, *Light: Science & Applications* **13**, 147 (2024).
- [11] Z. Wang, Z. Fang, Y. Zhu, J. Liu, L. Gao, J. Yu, H. Zhang, M. Wang, and Y. Cheng, An electro-optically tunable arrayed waveguide grating fabricated on thin film lithium niobate, *APL Photonics* **10** (2025).
- [12] C. Wang, Z. Li, J. Riemensberger, G. Lihachev, M. Churaev, W. Kao, X. Ji, J. Zhang, T. Blesin, A. Davydova, Y. Chen, K. Huang, X. Wang, X. Ou, and T. J. Kippenberg, Lithium tantalate photonic integrated circuits for volume manufacturing, *Nature* **629**, 784 (2024).
- [13] H. Hu, F. Da Ros, M. Pu, F. Ye, K. Ingerslev, E. Porto da Silva, M. Nooruzzaman, Y. Amma, Y. Sasaki, T. Mizuno, *et al.*, Single-source chip-based frequency comb enabling extreme parallel data transmission, *Nature Photonics* **12**, 469 (2018).
- [14] N. Picqué and T. W. Hänsch, Frequency comb spectroscopy, *Nature Photonics* **13**, 146 (2019).
- [15] J. Feldmann, N. Youngblood, M. Karpov, H. Gehring,

- X. Li, M. Stappers, M. Le Gallo, X. Fu, A. Lukashchuk, A. S. Raja, *et al.*, Parallel convolutional processing using an integrated photonic tensor core, *Nature* **589**, 52 (2021).
- [16] H. Ishio, J. Minowa, and K. Nosu, Review and status of wavelength-division-multiplexing technology and its application, *Journal of lightwave technology* **2**, 448 (1984).
- [17] M. Smit and C. Van Dam, PHASAR-based WDM-devices: Principles, design and applications, *IEEE Journal of Selected Topics in Quantum Electronics* **2**, 236 (1996).
- [18] M. K. Smit, New focusing and dispersive planar component based on an optical phased array, *Electronics letters* **24**, 385 (1988).
- [19] Y. Sano and T. Yoshino, Fast optical wavelength interrogator employing arrayed waveguide grating fordistributed fiber bragg grating sensors, *Journal of Lightwave Technology* **21**, 132 (2003).
- [20] A. Himeno, K. Kato, and T. Miya, Silica-based planar lightwave circuits, *IEEE Journal of Selected Topics in Quantum Electronics* **4**, 913 (1998).
- [21] N. A. Yebo, W. Bogaerts, Z. Hens, and R. Baets, On-Chip Arrayed Waveguide Grating Interrogated Silicon-Insulator Microring Resonator-Based Gas Sensor, *IEEE Photonics Technology Letters* **23**, 1505 (2011).
- [22] M. Piel, J. F. Bauters, M. L. Davenport, M. J. R. Heck, and J. E. Bowers, Low-Loss Silicon Nitride AWG Demultiplexer Heterogeneously Integrated With Hybrid III-V/Silicon Photodetectors, *Journal of Lightwave Technology* **32**, 817 (2014).
- [23] N. Keil, H. Yao, C. Zawadzki, J. Bauer, M. Bauer, C. Dreyer, and J. Schneider, Athermal polarization-independent all-polymer arrayed waveguide grating (awg) multi/demultiplexer, in *Optical Fiber Communication Conference* (Optica Publishing Group, 2001) p. PD7.
- [24] Y. Barbarin, X. Leijtens, E. Bente, C. Louzao, J. Kooiman, and M. Smit, Extremely small awg demultiplexer fabricated on inp by using a double-etch process, *IEEE Photonics Technology Letters* **16**, 2478 (2004).
- [25] D. Zhu, L. Shao, M. Yu, R. Cheng, B. Desiatov, C. Xin, Y. Hu, J. Holzgrafe, S. Ghosh, A. Shams-Ansari, *et al.*, Integrated photonics on thin-film lithium niobate, *Advances in Optics and Photonics* **13**, 242 (2021).
- [26] A. Boes, L. Chang, C. Langrock, M. Yu, M. Zhang, Q. Lin, M. Lončar, M. Fejer, J. Bowers, and A. Mitchell, Lithium niobate photonics: Unlocking the electromagnetic spectrum, *Science* **379**, eabj4396 (2023).
- [27] C. Wang, M. Zhang, X. Chen, M. Bertrand, A. Shams-Ansari, S. Chandrasekhar, P. Winzer, and M. Lončar, Integrated lithium niobate electro-optic modulators operating at CMOS-compatible voltages, *Nature* **562**, 101 (2018).
- [28] M. Xu, Y. Zhu, F. Pittalà, J. Tang, M. He, W. C. Ng, J. Wang, Z. Ruan, X. Tang, M. Kushnerov, *et al.*, Dual-polarization thin-film lithium niobate in-phase quadrature modulators for terabit-per-second transmission, *Optica* **9**, 61 (2022).
- [29] S. Ballandras, E. Courjon, F. Bernard, T. Laroche, A. Clairet, I. Radu, I. Huyet, A. Drouin, and E. Butaud, New generation of saw devices on advanced engineered substrates combining piezoelectric single crystals and silicon, in *2019 Joint Conference of the IEEE International Frequency Control Symposium and European Frequency and Time Forum (EFTF/IFC)* (IEEE, 2019) pp. 1–6.
- [30] C. Wang, D. Fang, J. Zhang, A. Kotz, G. Lihachev, M. Churaev, Z. Li, A. Schwarzenberger, X. Ou, C. Koos, *et al.*, Ultrabroadband thin-film lithium tantalate modulator for high-speed communications, *Optica* **11**, 1614 (2024).
- [31] K. Powell, X. Li, D. Assumpcao, L. Magalhães, N. Sinclair, and M. Lončar, Dc-stable electro-optic modulators using thin-film lithium tantalate, *Optics Express* **32**, 44115 (2024).
- [32] J. Zhang, C. Wang, C. Denney, J. Riemensberger, G. Lihachev, J. Hu, W. Kao, T. Blésin, N. Kuznetsov, Z. Li, M. Churaev, X. Ou, G. Santamaria-Botello, and T. J. Kippenberg, Ultrabroadband integrated electro-optic frequency comb in lithium tantalate, *Nature* **637**, 1096 (2025).
- [33] C. Dragone, An N*N optical multiplexer using a planar arrangement of two star couplers, *IEEE Photonics Technology Letters* **3**, 812 (2002).
- [34] P. Muñoz and J. Capmany, Modeling and Design of Arrayed Waveguide Gratings, *Journal of Lightwave Technology* **20** (2002).
- [35] H.-M. Zhang, C.-S. Ma, Z.-K. Qin, X.-Z. Zhang, Dan-Zhang, S.-Y. Liu, and D.-M. Zhang, Reduction of sidewall roughness, insertion loss and crosstalk of polymer arrayed waveguide grating using vapor-redissolution technique, *Thin Solid Films* **515**, 7313 (2007).
- [36] T. Ye, Y. Fu, L. Qiao, and T. Chu, Low-crosstalk Si arrayed waveguide grating with parabolic tapers, *Opt. Express* **22**, 31899 (2014), publisher: Optica Publishing Group.
- [37] X. Ji, J. Liu, J. He, R. N. Wang, Z. Qiu, J. Riemensberger, and T. J. Kippenberg, Compact, spatial-mode-interaction-free, ultralow-loss, nonlinear photonic integrated circuits, *Communications Physics* **5**, 84 (2022).
- [38] C. Wang, D. Fang, J. Zhang, A. Kotz, G. Lihachev, M. Churaev, Z. Li, A. Schwarzenberger, X. Ou, C. Koos, and T. J. Kippenberg, Ultrabroadband thin-film lithium tantalate modulator for high-speed communications, *Optica* **11**, 1614 (2024).
- [39] J. Liu, V. Brasch, M. H. Pfeiffer, A. Kordts, A. N. Kamel, H. Guo, M. Geiselmann, and T. J. Kippenberg, Frequency-comb-assisted broadband precision spectroscopy with cascaded diode lasers, *Optics Letters* **41**, 3134 (2016).
- [40] D. Seyringer, *Arrayed Waveguide Gratings* (SPIE, 2016).
- [41] C. Dragone, Efficient N*N star couplers using Fourier optics, *Journal of Lightwave Technology* **7**, 479 (1989).
- [42] M. Zhang, B. Buscaino, C. Wang, A. Shams-Ansari, C. Reimer, R. Zhu, J. M. Kahn, and M. Lončar, Broadband electro-optic frequency comb generation in a lithium niobate microring resonator, *Nature* **568**, 373 (2019).
- [43] M. Yu, D. Barton III, R. Cheng, C. Reimer, P. Kharel, L. He, L. Shao, D. Zhu, Y. Hu, H. R. Grant, *et al.*, Integrated femtosecond pulse generator on thin-film lithium niobate, *Nature* **612**, 252 (2022).
- [44] J. Riemensberger, A. Lukashchuk, M. Karpov, W. Weng, E. Lucas, J. Liu, and T. J. Kippenberg, Massively parallel coherent laser ranging using a soliton microcomb, *Nature* **581**, 164 (2020).
- [45] J. M. Lukens and P. Lougovski, Frequency-encoded photonic qubits for scalable quantum information processing, *Optica* **4**, 8 (2016).

- [46] S. Liu, R. Ma, W. Wang, Z. Yu, and D. Dai, Ultra-compact thin-film-lithium-niobate photonic chip for dispersion compensation, *Nanophotonics* **13**, 4723 (2024).
- [47] K. Ye, H. Feng, R. t. Morsche, A. Mishra, Y. Klaver, C. Wei, Z. Zheng, A. Keloth, A. T. Işık, Z. Chen, *et al.*, Brillouin photonics engine in the thin-film lithium niobate platform, *arXiv preprint arXiv:2411.06599* (2024).
- [48] F. Huang, X. Shen, S. Wang, H. Xu, H. Liu, Z. Wang, H. Gao, X. Yao, H. Cao, B. Chen, X. Wang, J. Zhang, Z. Wu, M. Zhu, H. Xiong, W. Zhao, H. Li, Z. Yu, L. Liu, Y. Shi, and D. Dai, Toward Large-Scale Photonic Chips Using Low-Anisotropy Thin-Film Lithium-Tantalate, *Advanced Science* **12**, 2410345 (2025).

Supplementary Information for: Arrayed waveguide gratings in lithium tantalate integrated photonics

Shivaprasad U. Hulyal¹, Jianqi Hu¹, Chengli Wang¹, Jiachen Cai¹, Grigory Lihachev¹, Tobias J. Kippenberg^{1,2}

¹*Institute of Physics, Swiss Federal Institute of Technology Lausanne (EPFL), CH-1015 Lausanne, Switzerland*

²*Institute of Electrical and Micro engineering, Swiss Federal Institute of Technology, Lausanne (EPFL), CH-1015 Lausanne, Switzerland*

Contents

| | |
|---|---|
| 1. Analytic simulation of AWG | 2 |
| A. Input Field as a Gaussian Beam | 2 |
| B. Propagation via Fresnel Diffraction | 3 |
| C. Coupling into Arrayed Waveguides | 3 |
| D. Phase Accumulation in Arrayed Waveguides | 3 |
| E. Interference in the Output Star Coupler | 3 |
| 2. Device parameters selection | 4 |
| 3. Parabolic taper design | 5 |
| 4. Wafer scale characterization of AWG | 5 |
| 5. Double Layer Taper design for AWG | 5 |

1. Analytic simulation of AWG

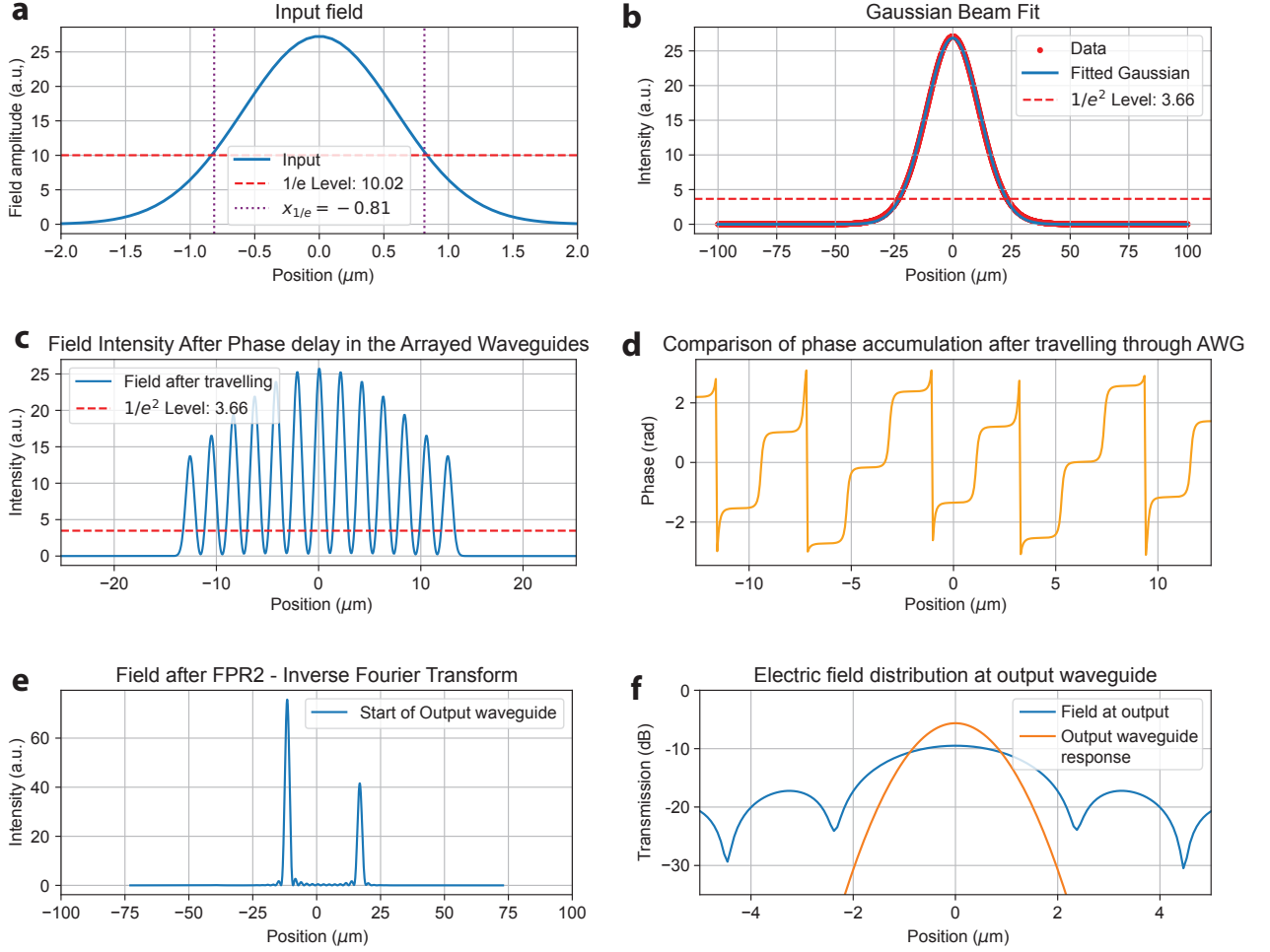


Figure S1. **Analytical simulation of AWG for the center channel.** (a) Gaussian beam at the start of input waveguide. (b) Expanded Gaussian beam after diffraction through the input star coupler. (c) Field intensity after coupling into arrayed waveguide and its corresponding intensity. (d) Phase accumulation after traveling through the delay lines. (e) Field amplitude at the output aperture. (f) Overlap between the output field intensity and the waveguide response for the central output waveguide.

We use a mathematical model implemented in Python to calculate and analyse the transmission spectrum of AWG.

A. Input Field as a Gaussian Beam

The input waveguide of an AWG supports a fundamental mode that can be approximated by a Gaussian beam profile as in Figure S1a. This Gaussian field represents the electric field distribution at the aperture of the input star coupler (free propagation region). In a planar waveguide geometry, assuming the mode is symmetric in the transverse (x, y) plane, the field at the star-coupler entrance (position $z = 0$) can be written as:

$$E_{\text{in}}(x) = E_0 \exp\left(-\frac{x^2}{w_0^2}\right) \quad (1)$$

where E_0 is the peak field amplitude and w_0 is the mode field radius (beam waist). Equation (1) is the standard Gaussian beam equation, capturing the fact that the field amplitude has a Gaussian transverse profile.

B. Propagation via Fresnel Diffraction

As the Gaussian beam propagates a distance z_1 through the input free propagation region (star coupler), it diffracts and broadens as shown in Figure S1b. The resulting field at the plane of the arrayed waveguides is calculated using the Fresnel diffraction integral:

$$E(x, z) = \frac{e^{ikz}}{i\lambda z} \int_{-\infty}^{\infty} E_{\text{in}}(x', 0) \exp\left[\frac{ik(x - x')^2}{2z}\right] dx' \quad (2)$$

where $E_{\text{in}}(x', 0)$ is the field at the input plane (given by the Gaussian of Eq. (1)), $k = 2\pi/\lambda$ is the wavenumber, and λ is the effective wavelength. Equation (2) is the Fresnel diffraction formula in one transverse dimension (here x) for the field at the array plane located a distance z from the input. This integral accounts for the diffraction spreading of the beam: each point x' in the input aperture contributes a spherical wave that interferes at observation point x . In the paraxial regime, the transformation from the input field to the focal plane field can be modeled as a spatial Fourier transform of the input distribution. [1]

$$E(x, z) = 1/\sqrt{b} \int_{-\infty}^{\infty} E_{\text{in}}(x', 0) \exp(j2\pi x' b x) dx' \quad (3)$$

where b is the scaling factor given by,

$$b = \frac{n_s v_0}{cz} \quad (4)$$

which holds in the region of Fraunhofer approximation.

$$z \gg \frac{\pi w_0^2}{4\lambda} \quad (5)$$

C. Coupling into Arrayed Waveguides

The diffracted field reaches the apertures of the arrayed waveguides, which are located at discrete positions x_n , where $n = 1, 2, \dots, N$. The amplitude coupled into the n -th waveguide is given by the overlap between the diffracted field and the mode profile $\psi_{\text{wg}}(x)$ of the waveguides:

$$a_n(\lambda) = \int_{-\infty}^{\infty} E(x, R_s) \psi_{\text{wg}}^*(x - x_n) dx \quad (6)$$

where R_s is the radius of the grating circle. This integral represents the excitation strength of each waveguide in the array, forming the input to the delay line network and the final field front is plot in Figure S1c.

D. Phase Accumulation in Arrayed Waveguides

A phase delay term is added to model the accumulated phase after traveling through the set of N delay lines. The pahse accumulated is plotted in Figure S1d.

$$\Phi_n(\lambda) = \frac{2\pi n_{\text{eff}}}{\lambda} (L_0 + (N - 1)\Delta L) \quad (7)$$

where n_{eff} is the effective refractive index of the waveguide and L_0 is the initial offset in the total length.

E. Interference in the Output Star Coupler

Each output waveguide is positioned at a specific $x = X_j$ to capture a particular wavelength's focal spot (channel j corresponds to a central wavelength λ_j). The coupling into an output waveguide is again given by an overlap integral between the field in the star coupler output plane and the mode of the output waveguide. The beams from the

arrayed waveguide interfere with each other in the output coupler and form a combined field distribution at the plane of the output waveguide array. This is shown in Figure S1e. Because each waveguide n has an amplitude a_n (from Eq. (6)) and a phase $\Phi_n(\lambda)$ (from Eq. (7)), the total electric field in the output coupler is the superposition of all N contributions. We can write the field at a position x in the output focal plane as:

$$E_{\text{out}}(x, \lambda) = \sum_{n=1}^N a_n(\lambda) e^{i\Phi_n(\lambda)} \psi_{\text{wg}}(x - x'_n) \quad (8)$$

The output star coupler can be considered to be as the interference from the different phase accumulated in the arrayed waveguides to focus the desired wavelength into the corresponding output waveguide.

The focused interference pattern in the output plane is collected by output waveguides located at positions X_j , corresponding to wavelength channels.

$$c_j(\lambda) = \int_{-\infty}^{\infty} E_{\text{out}}(x, \lambda) \psi_{\text{wg}}^*(x - X_j) dx \quad (9)$$

Figure S1f shows the overlap of the field intensity of output star coupler and the response of a single waveguide. The amount of power coupled into the j -th output waveguide is given by the overlap integral:

$$P_j(\lambda) = |c_j(\lambda)|^2 \quad (10)$$

2. Device parameters selection

The radius (R_a) of the input grating circle is chosen to accommodate the total number of arrayed waveguides which can be hence calculated as,

$$R_a = \frac{d_a N}{\theta_{da}} \quad (11)$$

where d_a is the spacing between the arrayed waveguides and θ_{da} is the width of the Gaussian far field. A larger number of arrayed waveguides reduces the bandwidth of the individual channels whereas a larger gap between the adjacent arrayed waveguides increases the insertion loss.

Efficient focusing of the propagating optical fields is achieved when the path length difference ΔL between adjacent waveguides corresponds to an integer multiple m of the effective wavelength within the waveguide medium.

$$\Delta L = m \cdot \frac{\lambda_c}{n_g} \quad (12)$$

Here ΔL is the length difference between adjacent arrayed waveguides and λ_c is the center channel wavelength, n_g is the group index of the material at a particular frequency (v), given by,

$$n_g = n_{\text{eff}} + v \frac{dn_{\text{eff}}}{dv} \quad (13)$$

The free spectral range (FSR) is related to the so-called order m of the AWG by and is chosen to fit all the channels of an AWG,

$$m = \frac{n_{\text{eff}}}{n_g} \frac{v_c}{v_{\text{FSR}}} \quad (14)$$

The dispersion (D) of the array defined as the lateral displacement (ds) of the focal spot along the image plane per unit frequency change [2], determines the spacing of the output waveguides (d_o),

$$D = \frac{ds}{dv} = \frac{1}{v_c} \frac{n_g}{n_{\text{FSR}}} \cdot \frac{\Delta L}{\Delta \alpha} \quad (15)$$

where $\Delta \alpha$ is the divergence angle of the set of arrayed waveguides, defined as,

$$\Delta \alpha = d_a / R_a \quad (16)$$

The parameters used for the AWG fabricated in the main text are listed in Table S1,

| Configuration | m | N | ΔL (μm) | w_a (μm) | d_a (μm) | R_a (μm) | w_o (μm) | d_o (μm) |
|---------------------------------------|-----|-----|------------------------|-------------------|-------------------|-------------------|-------------------|-------------------|
| Confocal: $1 \times 8 \times 100$ GHz | 160 | 13 | 129.7 | 1.6 | 2.1 | 75 | 2.0 | 2.9 |
| Rowland: $1 \times 8 \times 100$ GHz | 160 | 13 | 129.0 | 1.8 | 2.3 | 75 | 1.8 | 2.6 |

Table S1. Design parameters of the fabricated AWG

3. Parabolic taper design

Within the AWG framework, the implementation of adiabatic tapers is an effective strategy to minimize coupling losses between single-mode waveguides and the free propagation region (FPR), thereby enhancing overall device performance. Here we employ a parabolic taper design with to convert the mode from $2 \mu m$ to the fundamental mode of $1.6 \mu m$ ($1.8 \mu m$) for the Confocal (Rowland) type configuration on a 300 nm partially LiTaO₃ platform over a length of $5 \mu m$. The parabolic design follows the equation:

$$y = a(L_{taper} - x)^n + b \quad (17)$$

where L_{taper} is the length of the taper, and n is the power of the exponent. a and b are two constants determined by input and output waveguide width. $n = 2$ for the parabolic taper demonstrated an excellent reduced coupling loss at the interface of the star couplers and arrayed waveguides and hence the total insertion loss. Extensive research in taper design has led to various configurations optimized for efficient mode transformation across multiple photonic platforms, such as silicon [3] and silicon nitride [4].

4. Wafer scale characterization of AWG

We characterized the AWGs across multiple chips and fields on the wafer, with the results presented in Figure S2. For the Confocal AWGs, we measured an average insertion loss of 5.02 ± 1.06 dB, 3-dB bandwidth of 103.75 ± 9.80 GHz, adjacent channel crosstalk of -12.98 ± 3.39 dB, and a measured channel spacing of 104.64 ± 10.59 GHz. All values are reported with one standard deviation. In comparison, the spectra of the Rowland-type AWGs exhibited an insertion loss of $3.53 \text{ dB} \pm 0.69$, 3-dB bandwidth of 93.96 ± 15.51 GHz, adjacent channel crosstalk of -14.27 ± 2.13 dB, and a channel spacing of 114.98 ± 14.87 GHz, also reported with one standard deviation uncertainty.

The non-uniformity loss in AWGs arises from variations in output power across different channels and also from fiber-to-chip coupling. Comparing the two different designs fabricated, Rowland AWGs offer better performance in terms of uniformity (Figure S3).

5. Double Layer Taper design for AWG

Efficient optical coupling between the LiTaO₃ waveguide and the mode from the lensed fiber is achieved using double-layered waveguide tapers. In this design, the waveguide width is linearly reduced from the standard width to $0.16 \mu m$ over a length of $160 \mu m$. Beyond this point, the waveguide is cut off, and the underlying slab continues with a linear taper from its initial width down to $0.16 \mu m$ over an additional $100 \mu m$, terminating at the chip facet. This taper was patterned using electron beam lithography. This double-tapered structure facilitates low-loss mode matching with the lensed fiber. The coupling efficiency from the lensed fiber mode and LiTaO₃ taper mode can be estimated by mode overlap integral:

$$\eta = \frac{|\int_A E_{\text{lensed fiber}}^* \cdot E_{\text{taper}} dA|^2}{\int_A |E_{\text{lensed fiber}}|^2 dA \cdot \int_A |E_{\text{taper}}|^2 dA}, \quad (18)$$

where $E_{\text{lensed fiber}}$ is the mode field distribution at the lensed fiber and E_{taper} is the field distribution of the LiTaO₃ taper [5].

We designed double layer tapered edge couplers to couple light into the chip (Figure S4). The taper exhibits a linear transition from the 300 nm slab to the 600 nm waveguide core height over a length of $250 \mu m$. Edge couplers enable lower insertion losses due to their direct butt-coupling configuration, which minimizes scattering and diffraction losses that are often encountered in grating coupler structures. This direct interface facilitates a more efficient transfer of optical power between the lensed fiber and the edge coupler.

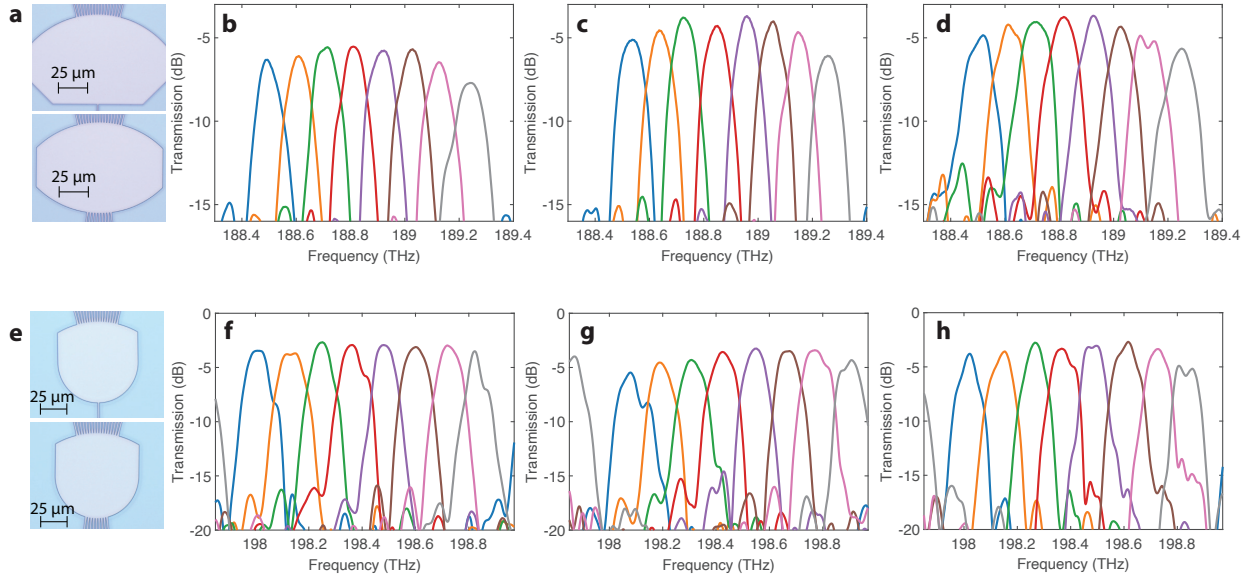


Figure S2. **Wafer scale AWG characterization results.** (a) Microscopic image of fabricated Confocal input star coupler (top) and output star coupler (bottom). Transmission spectrum of AWG with Confocal star coupler (Device ID: D197_C1.WG_203) across different fields of the wafer - (b) F5, (c) F1, (d) F3. (e) Microscopic image of fabricated Rowland input star coupler (top) and output star coupler (bottom). Transmission spectrum of AWG with Rowland star coupler (Device ID: D197_C6.WG_301) across different fields of the wafer - (f) F1, (g) F4, (h) F6.

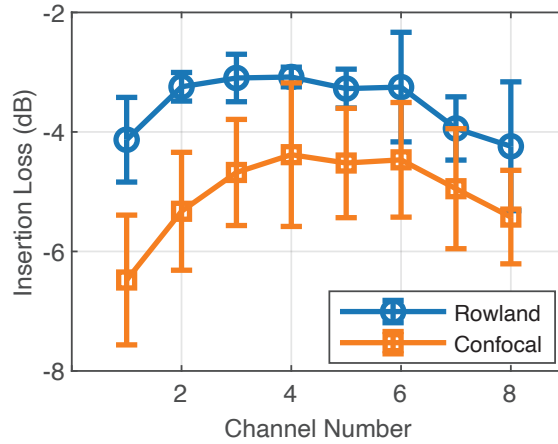


Figure S3. **Non-uniformity loss of Rowland and Confocal AWGs.** Insertion loss plotted as a function of channel number. Error bars represent the standard deviation calculated from measurements across the three AWGs, shown in Figure S2.

Supplementary References

- [1] M. Parker and S. Walker, *IEEE Journal of Selected Topics in Quantum Electronics* **5**, 1379 (1999).
- [2] M. Smit and C. Van Dam, *IEEE Journal of Selected Topics in Quantum Electronics* **2**, 236 (1996).
- [3] T. Ye, Y. Fu, L. Qiao, and T. Chu, *Opt. Express* **22**, 31899 (2014), publisher: Optica Publishing Group.
- [4] Z. Zhang, Y. Wang, and H. K. Tsang, *IEEE Journal of Quantum Electronics* **56**, 1 (2020).
- [5] M. W. Puckett and N. A. Krueger, *Applied Optics* **60**, 4340 (2021).

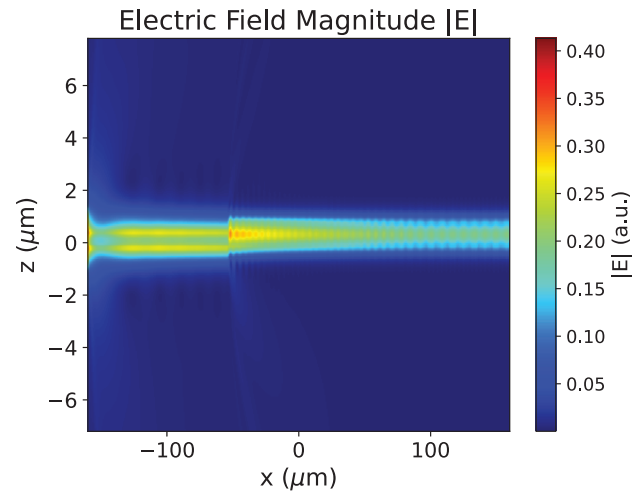


Figure S4. **FDTD simulations of double layer taper.** Electric field distribution showing the coupling of the mode from lensed fiber to the slab and then to the waveguide.